JOURNAL OF APPLIED CRYSTALLOGRAPHY

ISSN 1600-5767

Received 22 December 2014
Accepted 1 June 2015

Edited by J. Hajdu, Uppsala University, Sweden

# Low-*Z* polymer sample supports for fixed-target serial femtosecond X-ray crystallography

**Geoffrey K. Feld,[a]‡§ Michael Heymann,[b]‡¶ W. Henry Benner,[a] Tommaso Pardini,[a] Ching-Ju Tsai,[c] Sébastien Boutet,[d] Matthew A. Coleman,[a] Mark S. Hunter,[a]‡‡ Xiaodan Li,[c] Marc Messerschmidt,[d]§§ Achini Opthalage,[e] Bill Pedrini,[f] Garth J. Williams,[d]¶¶ Bryan A. Krantz,[g] Seth Fraden,[e] Stefan Hau-Riege,[a] James E. Evans,[h] Brent W. Segelke[a] and Matthias Frank[a]***

[a]Physical and Life Sciences Directorate, Lawrence Livermore National Laboratory, 7000 East Avenue, Livermore, CA 94550, USA, [b]Biophysics and Structural Biology Program, Graduate School of Arts and Science, Brandeis University, Waltham, MA, USA, [c]Laboratory of Biomolecular Research, Paul Scherrer Institute, Villigen, Switzerland, [d]Linac Coherent Light Source, SLAC National Accelerator Center, Menlo Park, CA, USA, [e]Martin A. Fisher School of Physics, Brandeis University, Waltham, MA, USA, [f]SwissFEL Project, Paul Scherrer Institute, Villigen, Switzerland, [g]Departments of Chemistry and Molecular and Cell Biology, University of California, Berkeley, CA, USA, and [h]Environmental Molecular Sciences Laboratory, Pacific Northwest National Laboratory, Richland, WA, USA. *Correspondence e-mail: frank1@llnl.gov

‡ These authors contributed equally to this work.
§ Present address: Genome Integrity and Structural Biology Laboratory, National Institute of Environmental Health Science, Research Triangle Park, NC, USA.
¶ Present address: Center for Free Electron Laser Science, University of Hamburg and DESY, Hamburg, Germany.
‡‡ Present address: Linac Coherent Light Source, SLAC National Accelerator Center, Menlo Park, CA, USA.
§§ Present address: BioXFEL Science and Technology Center, Buffalo, NY, USA.
¶¶ Present address: Brookhaven National Laboratory, Upton, NY, USA.

**Keywords:** X-ray free-electron lasers; biological crystallography; two-dimensional crystallography; microcrystallography; serial femtosecond crystallography.

X-ray free-electron lasers (XFELs) offer a new avenue to the structural probing of complex materials, including biomolecules. Delivery of precious sample to the XFEL beam is a key consideration, as the sample of interest must be serially replaced after each destructive pulse. The fixed-target approach to sample delivery involves depositing samples on a thin-film support and subsequent serial introduction *via* a translating stage. Some classes of biological materials, including two-dimensional protein crystals, must be introduced on fixed-target supports, as they require a flat surface to prevent sample wrinkling. A series of wafer and transmission electron microscopy (TEM)-style grid supports constructed of low-*Z* plastic have been custom-designed and produced. Aluminium TEM grid holders were engineered, capable of delivering up to 20 different conventional or plastic TEM grids using fixed-target stages available at the Linac Coherent Light Source (LCLS). As proof-of-principle, X-ray diffraction has been demonstrated from two-dimensional crystals of bacteriorhodopsin and three-dimensional crystals of anthrax toxin protective antigen mounted on these supports at the LCLS. The benefits and limitations of these low-*Z* fixed-target supports are discussed; it is the authors' belief that they represent a viable and efficient alternative to previously reported fixed-target supports for conducting diffraction studies with XFELs.

## 1. Introduction

The recent availability of X-ray free-electron laser (XFEL) light sources has extended the ability of X-rays to probe biomolecular structure (Chapman *et al.*, 2011; Seibert *et al.*, 2011; Feld & Frank, 2014; Spence *et al.*, 2012). The high X-ray flux ($10^{12}$ photons) and ultrashort (30 fs) durations of XFEL pulses enable data collection from smaller crystals and of shorter temporal resolution than other crystallographic methods. Beginning with three-dimensional nanocrystals of Photosystem I (Chapman *et al.*, 2011), increases in X-ray energy coupled with advances in experimental apparatus have incrementally added high resolution (Boutet *et al.*, 2012), previously unknown structures (Redecke *et al.*, 2012), *de novo* phasing (Barends *et al.*, 2014) and light-induced pump–probe capabilities (Aquila *et al.*, 2012; Kern *et al.*, 2013; Kupitz *et al.*, 2014; Tenboer *et al.*, 2014) to the structural biology XFEL toolbox.

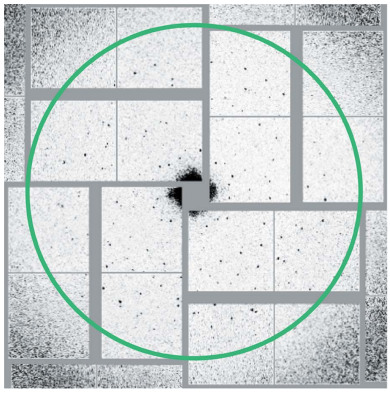

Because XFEL bio-imaging experiments rely on the 'diffraction-before-destruction' principle (Neutze *et al.*, 2000), a single specimen, such as a single molecule, three-dimensional or two-dimensional crystal, can only give rise to one diffraction pattern. Consequently, fresh sample must be serially delivered to the XFEL pulse. Lomb *et al.* coined the term 'serial femtosecond crystallography' (SFX), referring to an experiment performed with crystals of biological macromolecules (Chapman *et al.*, 2011; Lomb *et al.*, 2011). The gas dynamic virtual nozzle (GDVN), the first delivery mechanism for SFX, successfully injects fully hydrated crystals into the XFEL beam (Weierstall *et al.*, 2012); however, the fast linear velocity ($\geq$10 m s$^{-1}$) required to maintain a stable jet results in only an exceedingly small fraction (<0.1%) of the sample being probed by X-rays at 120 Hz, as this is the fastest repetition rate of the Linac Coherent Light Source (LCLS). This in turn leads to significant sample consumption requirements to complete an SFX experiment. One solution to this sample consumption dilemma is manifested in a lipidic cubic phase (LCP) injector, whereby crystals suspended in viscous LCP extrude from the injector at a significantly reduced velocity (Weierstall *et al.*, 2014). However, the applicable sample space with this injector is limited to LCP-compatible biological systems, namely integral membrane proteins. Furthermore, neither GDVN nor LCP injection technologies are appropriate for two-dimensional crystallography (2DX), which requires crystals to be kept relatively flat, generally on a support. 2DX represents an attractive method for structure determination of biomolecules, especially membrane proteins, given the reduced amount of sample required to form two-dimensional crystals and the near-native environment provided by a planar lipid bilayer (Wisedchaisri & Gonen, 2013). Another strategy, fixed-target serial femtosecond crystallography (FT-SFX), accomplishes both a reduction in sample consumption (Hunter *et al.*, 2014) and sample presentation on a flat surface at a fixed and known angle. For a typical FT-SFX experiment, samples are deposited on a wafer containing X-ray transmissible windows consisting of a thin film or membrane, *e.g.* 20–50 nm-thick $Si_3N_4$, and serially introduced into the beam *via* a translating stage (Hunter *et al.*, 2014; Frank *et al.*, 2014; Pedrini *et al.*, 2014).

Radiation damage associated with the long exposure times required at conventional X-ray sources (synchrotron and home source) prohibits structure determination by X-ray diffraction in transmission from two-dimensional lattices. On the other hand, the shallow penetration of electrons in biological materials limits their utility for three-dimensional crystallography (3DX) (Henderson, 1995). Thus, in general, transmission electron microscopy (TEM) enables 2DX while X-rays are used in 3DX. Using an FT-SFX approach, X-ray diffraction in transmission from two-dimensional crystals was recently demonstrated for the first time (Frank *et al.*, 2014) to ~7 Å resolution (Pedrini *et al.*, 2014), using the membrane protein bacteriorhodopsin (bR). Furthermore, the recent demonstration of electron diffraction from sub-micrometre three-dimensional crystals of lysozyme (microED) and subsequent structure solution has extended the capabilities of TEM (Shi *et al.*, 2013; Nannenga & Gonen, 2014). Therefore, the sample accessibility space for X-ray and electron diffraction is converging.

**Table 1**
Efficiency comparisons for fixed-target support materials.

| Support material | Acquisition time (min per 1000 shots) | Window density (shots cm$^{-2}$) | Sample consumption† (µl per 1000 shots) |
|---|---|---|---|
| $Si_3N_4$ wafer (100 ×100)‡ | 16 ± 1 | 310 | 7.7 |
| Metal grid (168)§ | 37 ± 4 | 538 | 11.9 |
| Plastic grid (64)§ | 65 ± 4 | 205 | 31.3 |
| Plastic grid (120)‡ | 40.4 ± 0.7 | 384 | 16.7 |
| Plastic grid (192)¶ | 25 | 614 | 10.4 |
| Plastic wafer (100 × 400)§ | 38 ± 2 | 522 | 4.6 |
| Plastic wafer (100 × 100)‡ | 15 ± 4 | 1567 | 1.5 |

† Assume 2 µl per 3.05 mm-diameter grid, 15 µl per 6.25 cm$^2$ wafer. For bR and PA, the starting concentrations of the proteins prior to crystallization are 1–3 mg ml$^{-1}$ and 26.5 mg ml$^{-1}$, respectively. ‡ Data collected in the 1.0 µm sample environment, July 2014. § Data collected in the 0.1 µm sample environment, May 2013. ¶ Numbers extrapolated from assuming the same shot per second rates achieved for 120 shot plastic grids.

In order to complement FT-SFX studies of two-dimensional and three-dimensional crystals, we have developed the tools and methodology to bridge XFEL and TEM techniques for sample preparation and delivery at XFELs. Here we report on the design, production and performance of low-*Z* polymer-constructed TEM-style mesh grids and wafers tailored to XFEL experiments. We constructed a fixed-target sample support holder capable of delivering up to 20 polymer TEM grids, as well as conventional (metal mesh) grids, for data collection, taking advantage of the ability of FT-SFX to deliver samples at a known angle and reduced sample consumption. Proof-of-principle X-ray diffraction experiments were conducted using both 0.1 and 1 µm beam focus sample environments of the Coherent X-ray Imaging (CXI) instrument (Boutet & Williams, 2010; Liang *et al.*, 2015) at the LCLS.

## 2. Design and construction

Two important considerations for FT-SFX include minimizing sample consumption (volume per shot) and maximizing the data acquisition (DAQ) rate (shots per time). Because these experiments are conducted under vacuum (~$10^{-6}$ Torr; 1 Torr = 133.322 Pa) in a chamber of limited size, overall DAQ rates are further constrained by the time required to vent and pump down for each sample change. Thus, for a given sample set, DAQ efficiency is also dependent on window density (shots per area) (Table 1). For a typical FT-SFX experiment, samples are deposited on individual support wafers with footprints of 25 × 25 mm or 25 × 12.5 mm. These wafers are then mounted on a fixed-target apparatus consisting of ~7500 mm$^2$ of X-ray accessible space (as of July 2014). Stepper motors control the *x*, *y* and *z* translation, as well as the tilt angle around the *x* axis. DAQ rates of ~10 per second have been shown for three-dimensional crystals on longer windows (Hunter *et al.*, 2014); however, under the allowed experimental conditions and considerations observed in this report,

DAQ is generally limited to shot-on-demand mode for two-dimensional crystals on fixed targets, ~1–2 per second, as each individual window must be translated and aligned with the beam.

In developing a suite of sample support devices for FT-SFX, we strove to reconcile traditional TEM sample preparation methods with the FT-SFX experimental constraints mentioned above. We surmised that sample consumption and window density could be simultaneously addressed using a canonical TEM grid, which requires only a minute sample volume (~2 µl) and small linear footprint (3.05 mm diameter). Most commercially available TEM grids are fabricated from a conductive metal to alleviate specimen charging during electron exposure (Egerton *et al.*, 2004) and are varied in terms of material composition and mesh size. For our design model, we considered tabbed (alias, 'handle') grids to exploit the additional tab bulk in orienting the grid for optimized data acquisition. We chose the Veco handle 150 copper square mesh grid with window dimensions 127 µm on an edge and a bar width of 40 µm. The relatively large hole provides some leeway for alignment, beam wings or other experimental factors that would lead to intense X-ray scattering from the copper mesh. Grids were custom-ordered pre-deposited with ~5 nm-thick carbon support film (Electron Microscopy Sciences, Hatfield, PA, USA).

### 2.1. Design and fabrication of plastic grid and wafer components

Since diffraction by X-rays is not limited by sample charging during exposure as it is for TEM, the construction of support grids from a conducting metal is superfluous. Indeed, replacing the metal with a lower-$Z$ polymer alleviates many of the concerns of the intense X-ray beam scattering from the metal support. We used SU8-photoresist (MicroChem Inc., Westborough, MA, USA) as the substrate for a polymer-constructed sample support. SU8-photoresist provides for the possibility of inexpensively mass producing an optimized design for potential high-throughput SFX applications. To ensure mechanical stability and maintain two-dimensional crystal sample flatness, we used a two-layer design of ~225 µm total thickness (Fig. 1*a*, see description below). We designed and fabricated our initial polymer grid (referred to herein as 'plastic grid') with the same footprint as the Veco handle grid described above (Fig. 1*b*). These grids have windows of dimensions 127 × 127 µm with separating bars of thickness 40 µm, giving rise to 120 full windows that are X-ray accessible (using either the 0.1 or 1 µm foci of the CXI).

Inspired by the rectangular design and subsequent high window density of the conventional $Si_3N_4$ sample support wafers employed in the initial FT-SFX experiments at the CXI (Frank *et al.*, 2014; Pedrini *et al.*, 2014; Hunter *et al.*, 2014), we also fabricated a wafer from SU8-photoresist (referred to herein as 'plastic wafer') in a similar manner to the plastic grids (Fig. 1*c*). These wafers have a 25 × 12.5 mm footprint, and their thicker SU8 support component consists of 17 × 8 units containing smaller XFEL-accessible windows, creating a 'window-in-a-window' design. While the added support restricts the available window space, this design still permits thousands of shots per wafer, depending on the window dimensions chosen. For example, the 100 × 100 µm window design we fabricated with 50 µm spacing provides 4896 X-ray-

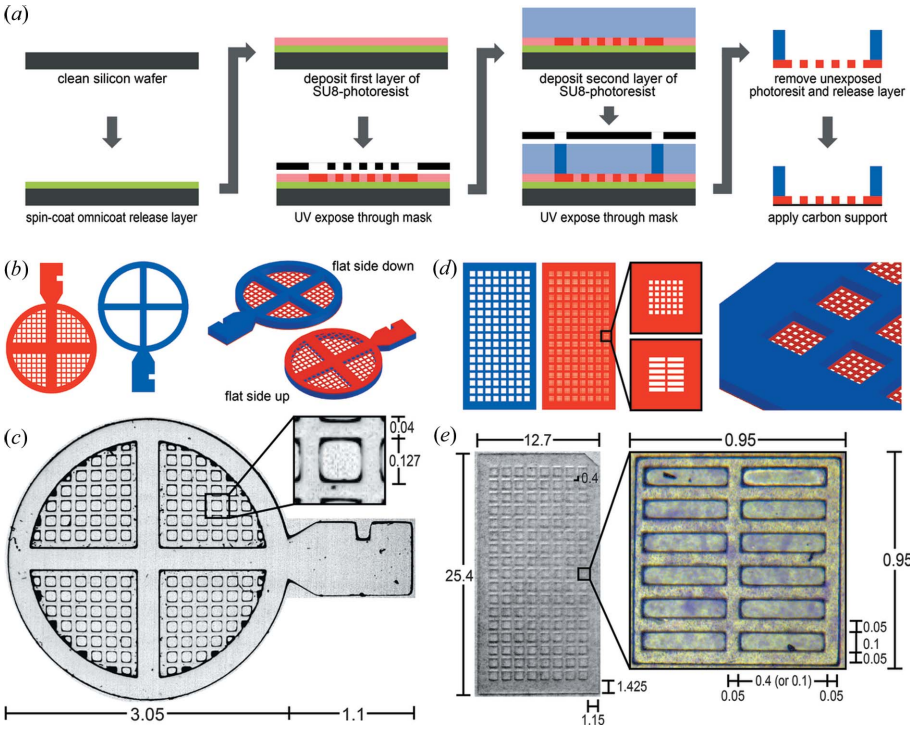


**Figure 1**
Fabrication and layout schematics of the plastic component. (*a*) Schematic of the fabrication process. After an Omnicoat release layer (green) a 25 µm layer of photoresist (red) is deposited and selectively cross-linked using UV light and a photomask. Subsequently a second 200 µm-thick layer of photoresist (blue) is deposited and patterned. Finally all uncured (unexposed) photoresist as well as the release layer are developed away and detached grids receive a carbon support to hold sample. (*b*) Plastic grid components rendered as CAD drawings. (*c*) Micrograph of an assembled plastic grid. The overall and window/bar dimensions are identical to the 150 mesh handle grid on which this particular design was based. (*d*) Wafer grid components rendered as CAD drawings. Both grids (*b*) and wafers (*d*) are constructed from two separate pieces, one containing the windows (red) and the other providing structural support (blue). Three-dimensional renderings of assembled grids (*a*), (right) and wafers (*d*), (right). (*e*) Micrograph of an assembled plastic wafer. The zoom-in micrograph shows the wafer used in this study with bR purple membrane adhered to carbon support with window dimensions 100 × 400 µm. Windows of dimensions 100 × 100 µm were also fabricated. All measurements are in mm.

accessible windows. By contrast, a comparable $Si_3N_4$ wafer of 44 rows and 18 columns contains only 792 windows (Table 1). Furthermore, compared to $Si_3N_4$ wafer fabrication, plastic grids are easier and faster to produce and hence allow for a more straightforward custom-design and fabrication platform of the window shape and dimension. The wafer in Fig. 1(*d*) contains windows of 100 × 400 µm, and windows of 100 × 100 µm were also fabricated and tested. One could conceive a 400 × 100 µm design for a 2DX tilt series, or a significantly longer window for fast FT-SFX data collection at ≥10 Hz (Hunter *et al.*, 2014).

Plastic grids and wafers were designed using the *AutoCAD* software suite (Autodesk, San Rafael, CA, USA) and translated into photo-masks through a commercial service (CAD/ART Services Inc., Bandon, OR, USA). They were then fabricated from SU8-photoresist on silicon wafers that were pre-treated to facilitate detaching of finished supports during SU8 development. A ∼28 nm-thick Omnicoat (MicroChem) release layer was prepared on the 3 inch (1 inch = 2.54 cm) polished wafer [P(100) 0–100 Ωcm SSP 380 µm Test Grade from University Wafer] by spin-coating at 500 r min$^{-1}$ for 5 s, followed by 3000 r min$^{-1}$ for 30 s, and then hard-baked at 473 K for 1 min. We then deposited a 25 µm layer SU8-3025 (MicroChem) for the window mesh followed by two additional SU8-2075 (MicroChem) layers of 100 µm thickness each for the support frame that reinforced the window mesh (Fig. 1*a*). This sequential build-up, rather than preparing a 200 µm film in a single step, was necessary to achieve the required accuracy for wafer thickness. Furthermore, the edge bead incurred from the sequential build-up was consistently smaller, allowing for more accurate alignment. Generally, SU8 layers were prepared by spin-coating and baking according to the manufacturer's specifications; however, some deviations were required to maintain accuracy for thickness and substrate flatness. These included spin-coating the second 100 µm layer onto the first 100 µm layer immediately after it had been soft-baked and doubling the UV exposure dose from 240 mJ cm$^{-2}$ recommended for 100 µm to 2 × 240 mJ cm$^{-2}$ for the 2 × 100 µm support frame. SU8 flows during the pre-exposure bake, resulting in a slight wedge-shaped cross section if it is not on a perfectly leveled surface. This effect is more pronounced at the longer baking times required for thicker layers. To further improve alignment accuracy of window mesh and support frame, we used a vernier caliper based alignment mark and a selective alignment mark development scheme (Heymann, Fraden *et al.*, 2014). After the final post-exposure bake, uncured SU8 and the Omnicoat release layer were developed away by washing in a bath of propylene glycol monomethyl ether acetate (Sigma–Aldrich, St Louis, MO, USA) overnight. The grids and wafers were then rinsed and stored in 2-propanol (Sigma–Aldrich) for transport.

The choice of support film to apply to plastic grids or wafers is experiment dependent. For initial experiments carried out at the LCLS, 8–20 nm-thick carbon films were floated onto the grids, either in bulk by lowering the film onto water-submerged grids, or individually by picking up 16 mm$^2$ carbon film pieces on 0.5–1 ml droplets of Milli-Q purified water (EMD Millipore, Billerica, MA, USA) and standard practices (Abeyrathne *et al.*, 2010). Carbon films of varying thickness, up to 20 nm, were applied to submerged plastic wafers by carefully lowering the film floating on a Milli-Q water surface. For three-dimensional microcrystal trials, we applied thin films of 1%(*w*/*v*) polyvinyl formal (in 1,2-dichloromethane) to plastic wafers at the air–water interface using standard methods.

### 2.2. Sample preparation and application

For our initial proof-of-principle FT-SFX studies of low-*Z* polymer supports, we used two-dimensional crystals of bR deposited on plastic grids and wafers. Preparation of purified bR patches followed methods reported previously (Frank *et al.*, 2014). Naturally occurring purple membrane (PM) from *Halobacterium salinarum* strain S9 was isolated, purified and treated with detergent to form single patches of two-dimensional crystals, as described elsewhere (Baldwin & Henderson, 1984; Henderson *et al.*, 1990). PM was diluted to 3 mg ml$^{-1}$ in a buffer containing 0.1 *M* potassium phosphate pH 5.2 (Sigma–Aldrich), 6 m*M* octyl glucoside (Avanti Polar Lipids Inc., Alabaster, AL, USA) and 200 µ*M* dodecyl trimethylammonium chloride (Sigma–Aldrich). Samples were then stored at room temperature for 24−72 h to allow for the membrane sheets to fuse and anneal. Next, bR patches were washed in water three times using a microcentrifuge at maximum speed to concentrate the material. Aliquots (2–3 µl) of 1–3 mg ml$^{-1}$ of bR were applied to the film side of UV-cleaned plastic grids sporting carbon support film by holding the grid in air with reverse forceps, allowing to air dry for 5 min and blotting away excess solution. Further applications of sugar embedding conditions, including up to 0.8%(*w*/*v*) glucose, to protect the sample from vacuum desiccation were also screened, as described elsewhere (Pedrini *et al.*, 2014; Henderson *et al.*, 1990); however, the data for these screens were not included in this report. Aliquots (2–3 µl) of bR were applied to a UV-cleaned plastic wafer dropwise, and subsequently spread with a 20/0 Royal sable artist paintbrush.

As proof-of-principle for FT-SFX studies of three-dimensional crystals on plastic wafer supports, we used a microcrystal–oil immersion technique as described previously (Hunter *et al.*, 2014). This sample consisted of three-dimensional microcrystals of the protective antigen (PA) component of anthrax toxin embedded in Paratone-N (Hampton Research, Hayward, CA, USA). While two-dimensional crystals of bR diffracted well *in vacuo* even without sugar embedding, we found that PA microcrystals are more sensitive to vacuum desiccation. Future work may establish better vacuum protection through screening of various sugars and sugar concentrations. A PA construct lacking its membrane insertion loop (PA$^{\Delta MIL}$) was bacterially expressed, purified and crystallized as described by Feld *et al.* (2012) using modifications to produce a large quantity of small (≤10 µm) crystals. PA$^{\Delta MIL}$ was overexpressed in *Escherichia coli,* purified by anion-exchange and size-exclusion chromatography in 0.02 *M* Tris–HCl pH 8.0, 0.15 *M* NaCl, concentrated to

26.5 mg ml$^{-1}$, and stored at 193 K. Free-interface batch crystallization of PA$^{\Delta MIL}$ was achieved in a 1.5 ml microcentrifuge tube by adding a 100 µl solution containing 50%(*v*/*v*) pentaerythritol ethoxylate (15:4 EO/OH, Sigma–Aldrich) and 0.1 *M* 2-[bis(2-hydroxyethyl)amino]-2-(hydroxymethyl)propane-1,3-diol HCl pH 6.7 to 100 µl protein solution at room temperature without mixing, followed by immediate plunging in an ice bath, and leaving the mixture to incubate overnight at 277 K. Further processing was conducted at room temperature; crystals were resuspended and filtered through a 10 µm cutoff 13 mm-diameter polycarbonate membrane (Sterlitech, Kent, WA, USA) prior to emulsification into Paratone. The crystal–oil immersion was adhered to plastic wafers sporting 1%(*w*/*v*) polyvinyl formal as the support layer by spreading with the edge of a 10 µl Rainin LTS pipette tip (Mettler–Toledo, Columbus, OH, USA).

### 2.3. TEM grid holder

With the goal of both adapting TEM grids to the CXI fixed-target sample holder and maintaining the flatness and integrity of the TEM grids, we designed a 25 × 25 mm TEM grid holder capable of carrying up to 20 mounted TEM handle grids. This holder was commercially machined from aluminium using standard computer numerical control milling (Concept Models, Livermore, CA, USA). The grid holder consists of two parts: a sample-loading bottom and a closing lid (Fig. 2*a*). The bottom contains etched depressions that snugly and specifically fit either metal (20 µm thick) or plastic (225 µm thick) grids mounted by hand, using forceps generally under a stereomicroscope. Owing to the fragility of the thin support film, we found it advantageous to mount grids with the thin-film substrate side up. The bottom of the grid holder is engineered to closely house tabbed TEM grids with the tabs pointed in either horizontal direction (Fig. 2*b*). In our hands, the thicker profile of the plastic grids enabled more facile substrate handling and mounting as the concern for grid bending is greatly diminished.

The lid design incorporates three primary aspects to facilitate the experiment. First, aluminium protrusions (∼100 µm long) on the lid's surface are designed to 'catch' complementary depressions on the bottom during assembly to ensure proper alignment (Fig. 2*c*). Second, the aluminium is machined at a 45° angle, so as to allow high-angle X-ray diffraction (Fig. 2*c*). Third, the lid is interchangeable with either sample-loading bottom that holds either the metal or plastic grid. Once grids are loaded, the handler carefully joins the bottom with the lid and secures the holder with 0–80 UNF flathead screws, producing a well protected array of up to 20 individually prepared TEM grids (Fig. 2*c*). The 25 × 25 mm footprint of the grid holder ensures its proper mounting in the CXI fixed-target sample holders (Fig. 2*d*).

## 3. X-ray diffraction data collection

To temporally and spatially couple the LCLS shots with motor function, we wrote scripts to initiate the XFEL pulse and

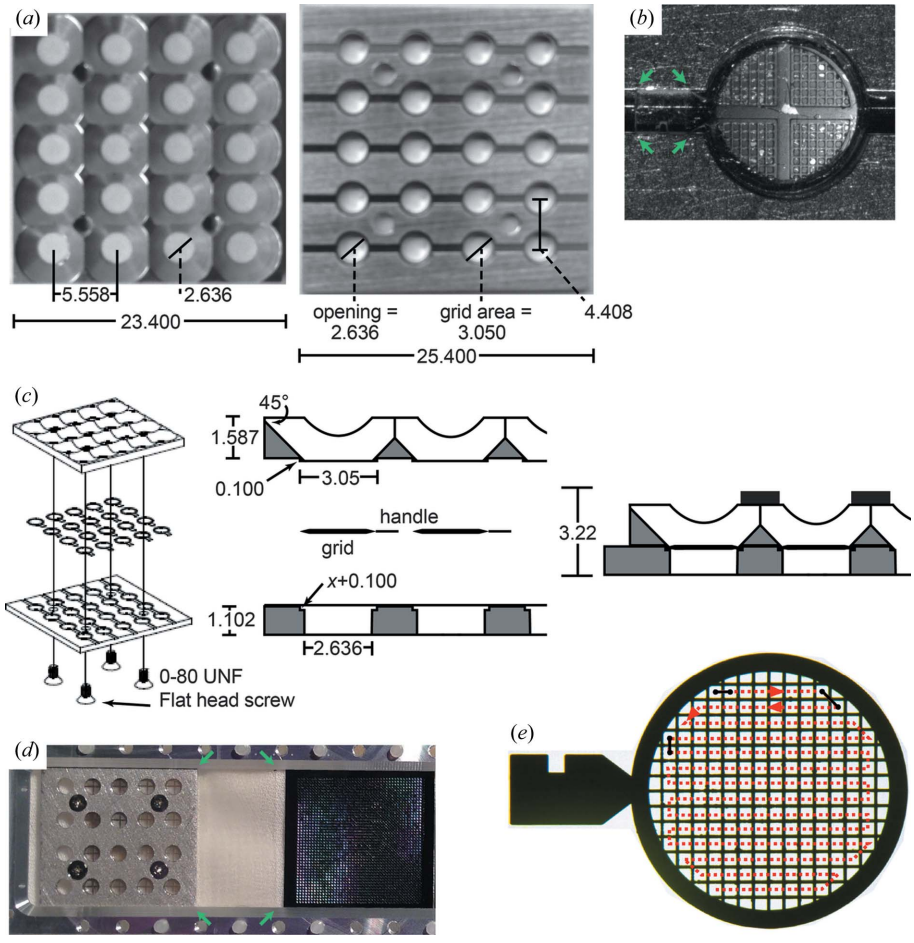


**Figure 2**
Aluminium grid holder for fixed-target XFEL sample delivery. (*a*) Photographs of grid holder components, lid (left, top view) and bottom (right, sample loading side, top view). (*b*) Micrograph of a mounted plastic grid with carbon substrate support. The construction permits handle grids to be placed in either horizontal orientation. The corners of the handle are indicated with green arrows. (*c*) Cartoon depiction of the grid holder assembly (left). Head-on cross sections through the grid holder components depict the dimensions and angles necessary for assembly (middle) as well as an assembled holder (right). While the lid is interchangeable with either grid type, bottom components are matched to the actual grid thickness; thus, *x* represents the thickness of either a plastic (0.225 mm) or metal (0.02 mm) grid. (*d*) Photograph of sample supports mounted on a CXI sample holder: grid holder filled with plastic grids (left), plastic wafer (middle) and $Si_3N_4$ wafer, July 2014. Green arrows indicate the corners of the translucent plastic wafer. (*e*) Micrograph of a Cu handle grid with an overlaid serpentine data collection scheme (red, dotted lines). Arrows indicate direction of raster, which is interchangeable, and solid lines (black) indicate stage translations. All measurements are in mm.

**Table 2**
Diffraction comparisons for plastic and metal mesh grids.

A 'hit' can correspond to a single crystal, a few crystals, many crystals (powder), a membrane with no crystal or unidentified 'junk'. Totals of 64 and 263 shots were recorded for the plastic and copper grids, respectively.

| Grid material | Total hits | Patterns with few lattices (%) | Patterns with powder rings (%) |
|---|---|---|---|
| Plastic | 25 | 40 | 0 |
| Copper | 263 | 1 | 82 |

subsequent stage translation (unpublished). A 'rastering' translation gives the fastest scanning geometry for circular TEM-style grids, where rows are shot sequentially, and each subsequent row is shot in the opposite direction in a serpentine pattern (Fig. 2*e*). Depending on which window is selected as the origin, this may proceed either 'up' or 'down' the grid. Generally, for each TEM grid, the *x* and *y* positions of the first and last window are recorded in a dry run, and the script is then used to compute precise *x* and *y* positions for all shots of the particular grid. The script then repositions the grid after each shot and triggers data acquisition.

DAQ statistics for the various sample support devices are summarized in Table 1. On average, one can expect a rate of ∼1 per second per window using either copper or plastic grids and a median deadtime between grids of 3 min. For 1000 shots, this extrapolates out to ∼2 s per shot. The DAQ rate for plastic wafer supported samples largely depends on the window density. Thus, the higher-density plastic wafer with window dimensions 100 × 100 µm attained a DAQ rate more than twice that observed for a plastic wafer with dimensions 100 × 400 µm. DAQ rates from samples supported by $Si_3N_4$ wafers are comparable to those from the plastic wafers, yielding ∼1 s per shot. The slower DAQ rate for copper and plastic grids is a direct result of the deadtime between grids; however, a hypothetical plastic grid with a higher window density could achieve DAQ rates approaching those of the larger wafers with fewer deadtimes.

The diffraction patterns obtained from two-dimensional bR crystals on TEM grids were consistent with patterns previously collected from two-dimensional bR crystals on $Si_3N_4$ (Frank *et al.*, 2014) or carbon (Pedrini *et al.*, 2014) window supports (Fig. 3). Patterns were collected on a single Cornell–SLAC Pixel Array Detector (CSPAD) at a nominal detector distance of ∼20 cm using 8.8 keV ∼30 fs LCLS X-rays at a pulse energy of ∼2 mJ (100% transmission). Crystal hits were identified in the raw data and converted to HDF5 file format using *Cheetah* (Barty *et al.*, 2014), and diffraction patterns were visualized using the *hdfsee* feature in *CrystFEL* (White *et al.*, 2012). For the two types of grids investigated, we identified strikingly different classes of diffraction patterns arising from two-dimensional bR crystals (Table 2). For the plastic TEM grids, all of the diffraction patterns contained sharp, distinguishable Bragg peaks consistent with either a small number of twinned lattices or single lattices (Fig. 3*a*). For the metal mesh grids, we observed only powder patterns almost exclusively, presumably arising from multiple lattice bR patches, and we did not identify any patterns approaching single lattices. These powder patterns roughly correlate with similar resolution limits as the fewer lattice patterns seen from bR on plastic grids (Fig. 3*b*). Previous work in the cryo-electron microscopy field has identified that membrane flatness is largely dictated by the composition of the grid support (Vonck, 2000), which

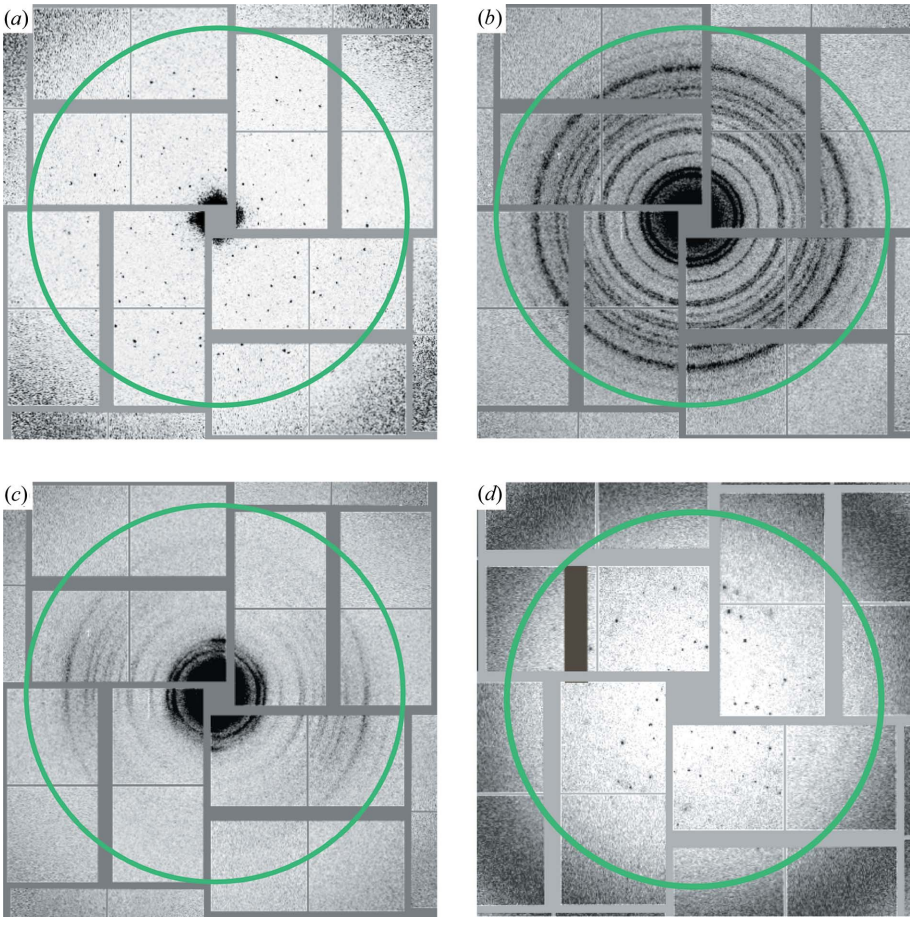


**Figure 3**
XFEL diffraction images of two-dimensional and three-dimensional crystals on sample supports. Green ring represents 7 Å in reciprocal space. Representative diffraction image from bR mounted on (*a*) a plastic grid with carbon support, (*b*) a Cu metal TEM grid with carbon support and (*c*) a plastic wafer with carbon support. Note the appearance of a tilted two-dimensional crystal at an unknown angle. (*d*) Representative diffraction image from $PA^{\Delta MIL}$ on a plastic wafer with polyvinyl formal support. Data were collected on a CSPAD detector at CXI, and images were produced using *hdfsee* in *CrystFEL* (White *et al.*, 2012).

can also affect sample binding efficiency. Thus the difference in quality and type of diffraction observed may be due to improved membrane flatness and uniform binding properties of the polymer grid supports (*i.e.* both the support and grid are constructed of carbonaceous material). However, owing to the small sample size of this study and our experience in optimizing sample concentration and preparation, we cannot rule out that sample variation may also contribute to the differences in quality and type of diffraction observed.

In our initial testing of the metal mesh grids, we observed sharp rings that probably correspond to X-ray scattering from copper at ∼2 Å (data not shown). With the detector close enough to record these rings, we were forced to operate using a significantly attenuated X-ray transmission. To mitigate the effects of copper scattering, we moved the detector out of range for the copper scattering angle. This poses an obvious drawback of the metal mesh grids for collecting high-resolution diffraction data. Interestingly, this X-ray scattering was observed using grids with window edges of 127 µm, although the X-ray focus was estimated to be ∼0.3 µm or smaller in diameter. Post-mortem inspection of these grids revealed that the LCLS beam was approximately centered in the window. We suspect that the X-ray beam profile had substantial flares well beyond the main focus of the beam that were intense enough to cause the observed copper scattering. It should also be noted that this scattering may be minimized with a secondary aperture.

For the plastic wafers, we tested both bR two-dimensional crystals as well as three-dimensional microcrystals of $PA^{\Delta MIL}$ embedded in Paratone-N. In these initial experiments we did not optimize the rigidity of the plastic wafers; the considerably larger plastic wafers noticeably bend in the long direction when mounted in the CXI fixed-target sample holder (the maximum radius of curvature is ∼1.5°, given that the wafers are still held securely on the sample holder). The curvature of the sample support is reflected in the diffraction patterns of bR two-dimensional crystals. The powder diffraction patterns, presumably arising from multi-layered bR two-dimensional crystal patches, resemble tilted data (note the tilt angle is unknown, Fig. 3*c*). However, FT-SFX of three-dimensional crystals should not require a flat substrate surface, as these crystals are not prone to bending or wrinkling. The diffraction patterns from three-dimensional microcrystals of $PA^{\Delta MIL}$ (similar experimental parameters as bR except the transmission was <1% and the detector distance was ∼17 cm) demonstrate sharp Bragg peaks with unit cells approximately the same as previously demonstrated with synchrotron X-rays at cryogenic temperatures (Feld *et al.*, 2012). Therefore, the superior shot density and sample consumption efficiency of the plastic wafers (Table 1) affirm their utility for FT-SFX of three-dimensional microcrystals, while, in the absence of further rigidifying support, they may not be suitable for FT-SFX of two-dimensional crystals.

## 4. Applications and discussion

Three important parameters affecting data collection for fixed-target serial femtosecond crystallography are DAQ rate, data accumulation between vacuum breaks and hits per quantity of sample. From the DAQ statistics (Table 1), both types of grids with window densities tested already surpass the shot densities for $Si_3N_4$ wafers; however, it is apparent that the limiting factor for data collection efficiency is the number of windows per grid, as the deadtime between grids is independent of grid type or window density. Future scripts that further automate the pre-collection alignment may decrease this deadtime, and the fabrication and successful testing of grids with higher window density are certainly conceivable. Thus, we expect that grid-based screening could rival wafers in terms of DAQ time and sample consumption efficiency. Given their high window density, reduced cost (when scaled up), and ease of fabrication and customizability, plastic wafers represent a competitive and viable alternative to $Si_3N_4$ wafers for three-dimensional FT-SFX. Further attempts to rigidify the plastic wafer design may enable their employment as sample supports for two-dimensional FT-SFX. Furthermore, these proof-of-principle experiments were conducted in shot-on-demand mode, limiting the maximum DAQ rate to ∼1–2 per second mode. We believe this is not a fundamental DAQ limit of the technique, as longer $Si_3N_4$ windows have enabled faster (∼10 per second) DAQ rates for three-dimensional crystals (Hunter *et al.*, 2014). While the use of longer windows has yet to be reported for two-dimensional crystals, it is not inconceivable that a similar advancement could be implemented for two-dimensional crystals.

In terms of the FT-SFX experimental approach, the grid-based sample substrate arrangement offers an intriguing advantage for screening diverse samples. As presented in Table 1, grids tested to date already provide a comparable window density to $Si_3N_4$ wafers, and further development should result in even higher densities. While wafer supports provide for more efficient sample consumption compared to the grids based on the designs tested here, these calculations assume one specific sample per wafer. The grid system permits a variety of samples to be screened, each with a minute sample volume requirement (∼2 µl per grid) and a different variable to compare. Grids were used to screen various sample conditions, including sugar embedding media and protein concentration, as well as different proteins and preparations at the CXI (data not shown). The ability to screen up to 20 different samples in a 25 × 25 mm footprint enables quick and efficient optimization for a larger or more sophisticated SFX experiment. The grid and holder system provides a useful avenue to quickly screen multiple samples and conditions during full or half-shift protein crystal screening experiments at the CXI. Moreover, serial room-temperature crystallography has recently gained traction at synchrotron X-ray sources (Soares *et al.*, 2014; Heymann, Opthalage *et al.*, 2014; Stellato *et al.*, 2014), and the plastic grids and wafers presented here should be adaptable to beamlines that take advantage of this methodology. Finally, our initial results suggest that the polymer grids may represent a superior platform for efficient sample spreading and binding, given the exceptionally high ratio of few/single lattices *versus* powder rings observed in the diffraction patterns (Table 2). A larger and more rigorous

side-by-side sampling is necessary to definitively make this distinction.

By developing an experimental setup that allows commonplace TEM supplies and procedures to be seamlessly integrated into XFEL sample introduction, we provide a means to unite these two diffraction methods. In this manner, samples may be assessed for quality using a transmission electron microscope prior to XFEL introduction on the same metal grids. Some XFEL instruments and end-stations, including the X-ray Pump Probe instrument at the LCLS and planned end-stations at the forthcoming European XFEL, can accommodate cryostages, providing further compatibility with cryo-TEM measurements. Here, we described viable plastic grids that may be specifically tailored for XFEL experiments without metal background scattering. We propose an experimental pipeline where samples are initially characterized by TEM using metal grids, which may be examined with XFELs for diffraction quality; further optimization under XFEL conditions is then screened with plastic grids designed specifically for the experiment under investigation. Furthermore, plastic grid designs that prove most useful for screening purposes can be easily and cheaply mass-produced for high-throughput operation. We foresee that the substrate support components and methods described here will provide a useful mechanism for extending the capabilities of FT-SFX at XFELs.

## Acknowledgements

GKF, WHB, BWS, JEE, SHR and MF proposed and outlined the research; GKF and MH conceived and designed the plastic support components; MH and AO fabricated the plastic supports under the supervision of SF; WHB, GKF and MF designed the grid holder; GKF, CJT, MAC, JEE, MH, BWS, BAK, MSH and XL provided and prepared samples; TP, SHR and GJW wrote and executed the rastering scripts; SB, GJW and MM operated the CXI instrument; GKF, MH, JEE, MSH, TP, SHR, MAC, BWS, SB, MM, GJW, CJT, BP, XL and MF collected diffraction data; GKF and JEE analyzed diffraction and DAQ data with input from BP and MSH; GKF, MH, BWS and MF wrote the manuscript with contributions from all authors. The authors acknowledge Dongshin Kim for help and discussions on grid fabrication, and Mukthi Kukkadapu and Emme Patello for sorting diffraction data. Work was performed under the auspices of the US Department of Energy by Lawrence Livermore National Laboratory under contract DE-AC52-07NA27344 and Pacific Northwest National Laboratory (operated by Battelle Memorial Institute) under contract DE-AC05-76RL01830. Support was provided by LLNL Lab-Directed Research and Development (LDRD) Project 12-ERD-031, the PNNL Chemical Imaging Initiative, and the NSF Brandeis MRSEC (DMR-0820492). Portions of this research were carried out at the Linac Coherent Light Source (LCLS) at SLAC National Accelerator Laboratory. LCLS is an Office of Science User Facility operated for the US Department of Energy Office of Science by Stanford University.

## References

Abeyrathne, P. D., Chami, M., Pantelic, R. S., Goldie, K. N. & Stahlberg, H. (2010). *Methods Enzymol.* **481**, 25–43.
Aquila, A. *et al.* (2012). *Opt. Express*, **20**, 2706–2716.
Baldwin, J. M. & Henderson, R. (1984). *Ultramicroscopy*, **14**, 319–335.
Barends, T. R., Foucar, L., Botha, S., Doak, R. B., Shoeman, R. L., Nass, K., Koglin, J. E., Williams, G. J., Boutet, S., Messerschmidt, M. & Schlichting, I. (2014). *Nature*, **505**, 244–247.
Barty, A., Kirian, R. A., Maia, F. R. N. C., Hantke, M., Yoon, C. H., White, T. A. & Chapman, H. (2014). *J. Appl. Cryst.* **47**, 1118–1131.
Boutet, S., Lomb, L. *et al.* (2012). *Science*, **337**, 362–364.
Boutet, S. & Williams, G. J. (2010). *New J. Phys.* **12**, 035024.
Chapman, H. N. *et al.* (2011). *Nature*, **470**, 73–77.
Egerton, R. F., Li, P. & Malac, M. (2004). *Micron*, **35**, 399–409.
Feld, G. K. & Frank, M. (2014). *Curr. Opin. Struct. Biol.* **27**, 69–78.
Feld, G. K., Kintzer, A. F., Tang, I. I., Thoren, K. L. & Krantz, B. A. (2012). *J. Mol. Biol.* **415**, 159–174.
Frank, M. *et al.* (2014). *IUCrJ*, **1**, 95–100.
Henderson, R. (1995). *Q. Rev. Biophys.* **28**, 171–193.
Henderson, R., Baldwin, J. M., Ceska, T. A., Zemlin, F., Beckmann, E. & Downing, K. H. (1990). *J. Mol. Biol.* **213**, 899–929.
Heymann, M., Fraden, S. & Kim, D. (2014). *J. Microelectromech. Syst.* **23**, 424–427.
Heymann, M., Opthalage, A., Wierman, J. L., Akella, S., Szebenyi, D. M. E., Gruner, S. M. & Fraden, S. (2014). *IUCrJ*, **1**, 349–360.
Hunter, M. S. *et al.* (2014). *Sci. Rep.* **4**, 6026.
Kern, J. *et al.* (2013). *Science*, **340**, 491–495.
Kupitz, C. *et al.* (2014). *Nature*, **513**, 261–265.
Liang, M. *et al.* (2015). *J. Synchrotron Rad.* **22**, 514–519.
Lomb, L. *et al.* (2011). *Phys. Rev. B*, **84**, 214111.
Nannenga, B. L. & Gonen, T. (2014). *Curr. Opin. Struct. Biol.* **27**, 24–31.
Neutze, R., Wouts, R., van der Spoel, D., Weckert, E. & Hajdu, J. (2000). *Nature*, **406**, 752–757.
Pedrini, B. *et al.* (2014). *Philos. Trans. R. Soc. London Ser. B*, **369**, 20130500.
Redecke, L. *et al.* (2012). *Science*, **339**, 227–230.
Seibert, M. M. *et al.* (2011). *Nature*, **470**, 78–81.
Shi, D., Nannenga, B. L., Iadanza, M. G. & Gonen, T. (2013). *eLife*, **2**, e01345.
Soares, A. S., Mullen, J. D., Parekh, R. M., McCarthy, G. S., Roessler, C. G., Jackimowicz, R., Skinner, J. M., Orville, A. M., Allaire, M. & Sweet, R. M. (2014). *J. Synchrotron Rad.* **21**, 1231–1239.
Spence, J. C. H., Weierstall, U. & Chapman, H. N. (2012). *Rep. Prog. Phys.* **75**, 102601.
Stellato, F. *et al.* (2014). *IUCrJ*, **1**, 204–212.
Tenboer, J. *et al.* (2014). *Science*, **346**, 1242–1246.
Vonck, J. (2000). *Ultramicroscopy*, **85**, 123–129.
Weierstall, U. *et al.* (2014). *Nat. Commun.* **5**, 3309.
Weierstall, U., Spence, J. C. & Doak, R. B. (2012). *Rev. Sci. Instrum.* **83**, 035108.
White, T. A., Kirian, R. A., Martin, A. V., Aquila, A., Nass, K., Barty, A. & Chapman, H. N. (2012). *J. Appl. Cryst.* **45**, 335–341.
Wisedchaisri, G. & Gonen, T. (2013). *Electron Crystallography of Soluble and Membrane Proteins*, Vol. 955, *Methods in Molecular Biology*, edited by I. Schmidt-Krey & Y. Cheng, pp. 243–272. Totowa: Humana Press.